Journal of Hazardous Materials Advances 10 (2023) 100273

Contents lists available at ScienceDirect

Journal of Hazardous Materials Advances

journal homepage: www.elsevier.com/locate/hazadv

Hydrothermal catalytic conversion of oleic acid to heptadecane over Ni/ZrO_2

L. Estelle Cronmiller[a], James M. Crawford[b], Jing Zhang[c], Derek R. Vardon[d], Timothy J. Strathmann[a,*]

[a] Department of Civil and Environmental Engineering, Colorado School of Mines, 1500 Illinois St., Golden CO 80401, USA
[b] National Renewable Energy Lab, 15103 Denver W Pkwy, Golden, CO 80401, USA
[c] School of Environment, Harbin Institute of Technology, Harbin 150090, China
[d] Alder Fuels, 2915 O Street North West, Washington, DC 20007, USA

ARTICLE INFO

Keywords:
Waste valorization
Subcritical
Linoleic acid
Drop-in fuel
Earth abundant metals

ABSTRACT

There is growing interest in the substitution of expensive noble metal catalysts with low-cost earth-abundant metals in applications targeting biofuels production from waste organic feedstocks. Here, nickel (Ni) catalysts supported on zirconium dioxide (ZrO_2), both with and without copper (Cu) as a co-metal, were tested in hydrothermal reactions of unsaturated and saturated C18 fatty acids as models for waste oil feedstocks. In contrast to recent reports, this study showed no enhancement of nickel's activity for fatty acid conversion to alkane products when Cu was present. Ni/ZrO_2 prepared by metal coprecipitation methods converted 100% of oleic acid with 25% selectivity to heptadecane after 5 h of reaction at 350 °C using methanol as a hydrogen donor source, increasing to 41% heptadecane after 20 h. Lower yields were observed with catalysts prepared by wet impregnation and using alternative hydrogen donor sources (glycerol, formic acid). Greater selectivity to heptadecane was also observed at higher temperatures (370 °C) and when the initial fatty acid had greater saturation. Longer term exposure to hydrothermal media led to metal sintering and catalyst deactivation. Findings support a path forward to the development of earth-abundant metal catalysts for the upgrading of waste organic feedstocks.

1. Introduction

Growing concerns about international dependencies and environmental impacts of fossil fuel sources are driving a national transition towards more sustainable and renewable energy sources, including bio-derived liquid fuels (Schiffer, 2022; O'Riordan and Sandford, 2022). Moreover, rising mobility demands are leading to intensified efforts to identify renewable drop-in replacements for both diesel and aviation fuel (Yan et al., 2021). The aviation industry in particular has high investment for biofuel substitutes considering electrification isn't as viable option for decarbonization as it is in the ground transportation sector. These shifting priorities are reflected in recent federal legislation that incentivizes biofuel production and use through tax credits and grants (Sustainable Aviation Fuel Grand Challenge, 2023; Brownley, 2023; Yarmuth, 2022). It follows that many groups are examining the potential of waste streams as reliable carbon sources that can serve a circular economic agenda (Awogbemi et al., 2021; Al-Muhtaseb et al., 2021). Among these, waste oils, fats and greases (e.g., used cooking oil) have drawn attention due to the high energy content and chemical similarity of long chain fatty acids to conventional diesel fuels (Borugadda and Dalai, 2018; Orsavova et al., 2015). Direct use of long chain fatty acids, and even their conversion to esterified biodiesel, is challenging due to flash point and viscosity discrepancies that limit mixing with or wholesale replacement of petroleum-derived fuels (Dey and Ray, 2020). However, fatty acid conversion to long-chain alkanes through deoxygenation and decarboxylation mechanisms offer potential for improved diesel engine compatibility with preferred ignition quality owing to their high cetane number (Yanowitz et al., 2017). This provides a compelling reason for identifying strategies for selectively deoxygenating fatty acids to hydrocarbons, especially fatty acids prevalent in food waste streams, e.g., oleic acid.

Adding to the challenge in deoxygenating fatty acids with conventional refinery catalysts, waste fatty acid streams are often characterized by high moisture contents (Peng et al., 2008; Lizhi et al., 2008; Peterson et al., 2008), and the hydrodeoxygenation process, itself, generates water as a stoichiometric byproduct. As a result, there has been

Abbreviations: $Ni-Cu/ZrO_2$, Nickel and copper on zirconium dioxide catalyst; Ni/ZrO_2, Nickel on zirconium dioxide catalyst; Cu/ZrO_2, Copper on zirconium dioxide catalyst; CP, Co-precipitated; WI, Wet impregnated; HD, Heptadecane; SA, Stearic acid; OA, Oleic acid; LA, Linoleic acid.

* Corresponding author.
E-mail address: strthmnn@mines.edu (T.J. Strathmann).

https://doi.org/10.1016/j.hazadv.2023.100273
Received 29 December 2022; Received in revised form 28 February 2023; Accepted 2 March 2023

significant efforts directed towards development and commercialization of aqueous-phase catalytic processes for conversion of fatty acids, most often performed under hydrothermal conditions (250–400 °C, 10–18 MPa) (Peterson et al., 2008; ReadiJet- ARA 2023). Using a suitable hydrogen source, fatty acids like oleic acid can be converted in hydrothermal media to linear alkanes by hydrogenation (Eq. (1a)) and decarboxylation (Eq. (1b)) mechanisms:

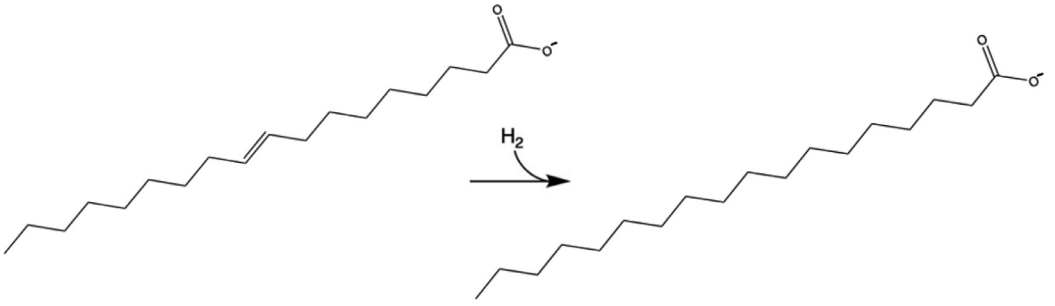

(1a)

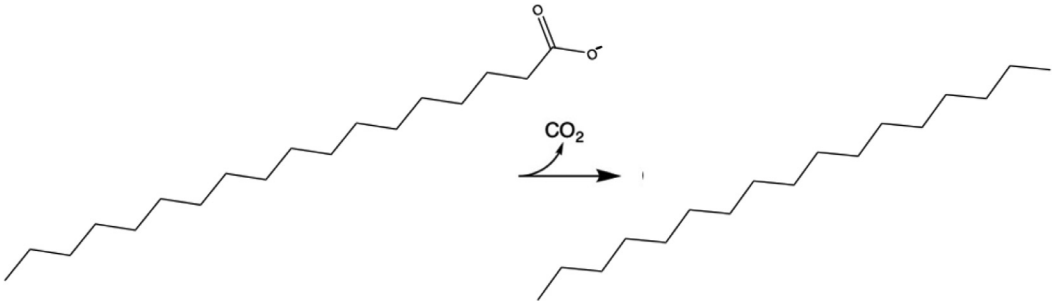

(1b)

While there is a growing number of reports on hydrothermal fatty acid-to-alkane conversion, most studies have employed expensive noble metal catalysts, including platinum, palladium, and rhodium (Mäki-Arvela et al., 2007; Murata et al., 2010). Recent costs of these active metals has ranged from $900 to 2400/oz (Daily Metal Price: Free Metal Price Tables and Charts 2023). Moreover, significant negative environmental impacts are often associated with mining and processing of these rare metals (Burnett et al., 2021; Amatayakul and Ramnäs, 2001), something that is counter to the broader sustainability goals of biorenewable fuels. Some of the present authors recently reported on successful hydrothermal fatty acid-to-hydrocarbon conversion using supported ruthenium catalysts as a lower cost noble metal substitute, but market prices for this metal have also grown dramatically in recent years, highlighting additional challenges associated with the price volatility of these trace metals.

The above discussion has led to renewed interest in identifying more earth-abundant and low-cost metals that might also be effective catalysts for hydrothermal fatty acid conversions. A recent report by Zhang et al. (2018a) showed hydrothermal conversion of oleic acid to heptadecane can be accomplished using a Ni-Cu bimetal catalyst supported on ZrO_2, where hydrogen was supplied by *in situ* aqueous phase reformation of methanol. Nickel and copper are priced at $0.74/oz and $0.25/oz, respectively, making them an obvious price cognizant replacement for aforementioned noble metals (Daily Metal Price: Free Metal Price Tables and Charts, 2023). ZrO_2 has shown promise as a stable support material for use in harsh hydrothermal environments (Papageridis et al., 2020; Joshi et al., 2014). Furthermore, zirconium may have a functional role in reactions since it has been shown to facilitate hydrogen production from water gas shift reactions of liquid hydrogen sources (Stekrova et al., 2018; Amatayakul and Ramnäs, 2001; Lytkina et al., 2015). Though Cu itself is not thought to be catalytic on its own, its interactions with Ni have been shown to enhance the latter's activity for a variety of upgrading processes, including gasification, hydrogenation and pyrolysis (Rashidi and Tavasoli, 2015; Wang et al., 2020; Kumar et al., 2019). For example, Luo et al. used core-shell structured Ni-Cu nanocrystals on a carbon support for hydrodeoxygenation of 5-hydroxymethylfurfural and showed that the incorporation of copper resulted in >30% higher selectivity for 2,5-dimethylfuran as compared to the corresponding supported Ni mono-metal catalyst (Stekrova et al., 2018; Luo et al., 2017). Modeling of this co-metal has shown its ability to increase the rate and selectivity of the water gas shift reaction, leading to higher H_2 production in aqueous systems (Stekrova et al., 2018; Lytkina et al., 2015; Gan et al., 2012) and promote active site clearing through carbon deposit oxidation (Stekrova et al., 2018; Boualouache and Boucenna, 2020).

The present report revisits the recent findings by Zhang and coworkers (Rashidi and Tavasoli, 2015; Zhang et al., 2018a) to further examine the reactions of oleic acid and related fatty acids (stearic acid and linoleic acid) over Ni- and Cu- catalysts in hydrothermal media. Surprisingly, initial experiments comparing mono-metal and bimetal catalysts activity show similar oleic acid conversion with Ni/ZrO_2 as $Ni\text{-}Cu/ZrO_2$, inspiring a deeper investigation of Ni/ZrO_2 reactivity. Thus, we conducted the first thorough evaluation of Ni/ZrO_2 for deoxygenation of multiple long-chain fatty acids under hydrothermal conditions. Method of catalyst preparation (co-precipitation versus wet impregnation), hydrogen source and concentration, and catalyst deactivation pathways were all studied. Through relation of the highest performing catalysts' abilities under incrementally changing conditions to their morphological distinctions, we build the foundation for more directed future catalyst design. Findings point to a path forward towards development of lower cost and more environmentally sustainable materials that will be critical to efforts targeting valorization of waste carbon streams like used oils, fats, and greases.

2. Experimental section

2.1. Reagents

Zirconyl(IV) nitrate hydrate (99.5%) was obtained from Acros Organics. Glycerol (ACS grade) was purchased from Merck. Sodium hy-

droxide (20 N) and methanol (optima grade) were obtained from Fisher Chemical. Boron trifluoride (20% in methanol solution), hexane (>97.0%), stearic acid (>98.5%), linoleic acid (99%), nickel(II) nitrate hexahydrate (>94.5%), copper(II) nitrate trihydrate (analysis grade), oleic acid (90%), ethylene glycol (>99%), glucose (>99.5%), formic acid solution (1 M), dichloromethane (>99.8%) and sodium carbonate (>99.5%) were obtained from Sigma-Aldrich.

2.2. Catalyst synthesis

Metal co-precipitation and wet impregnation methods were used to synthesize Ni- and Cu-based mono-metal and bimetal catalysts using tetragonal ZrO_2 as a hydrothermally stable support material. Co-precipitation methods were adapted from Zhang et al. (2018). A 0.1 M solution of metal precursors, with the final Cu, Ni, or Cu-Ni (1:1 molar ratio) loading of 15 wt% relative to Zr salt was mixed with a second solution containing 0.15 M NaOH and 0.045 M Na_2CO_3. The two solutions were mixed in a round bottom flask to obtain a pH of 9.5, and stirred at 1000 rpm overnight. The resulting solid was collected by vacuum filtration and washed with deionized water before drying in an oven for 12 h at 110 °C. Tetragonal ZrO_2 was synthesized in the same manner except that Ni and Cu salts were omitted from the preparation. Catalysts prepared by wet impregnation were synthesized using procedures adapted from previous reports (Freitas et al., 2018). Cu or Ni nitrate salt solutions (either 6.336 g Cu or 5.191 g Ni salts) were immobilized onto 6.667 g of the pre-synthesized tetragonal ZrO_2 support material in 50 mL of water while sonicating for 30 min, followed by stirring at room temperature overnight at 250 rpm. The resulting solid was recovered and washed three times with water and ethanol before drying in an oven at 110 °C for 12 h. Independent of synthesis procedure, dried catalysts were ground with a motor and pestle before calcining in a furnace at 600 °C for 4 h with 1 h ramp time. Following calcination, individual catalysts were activated in a tube furnace under flowing H_2 for 1 h at 650 °C after a 1 h ramp time (~10 °C/min).

2.3. Catalyst characterization

Elemental compositions of the catalysts and selected aqueous phase samples following oleic acid conversions were obtained by inductively coupled plasma-atomic emission spectrometry (ICP-AES; Perkin Elmer). Prior to analysis, solids (3.5 mg) were microwave digested in 3 ml HCl + 9 ml HNO_3 before diluting to 100 mL in deionized water for analysis. Phase composition was determined by X-ray diffraction (XRD, PANalytical PW3040 X-ray diffractometer) between 10 and 80° (2θ) at a scan rate of 37° min^{-1}. HighScore spectral analysis was used for spectrographic assurance. To supplement ICP-AES and XRD for compositional confirmation, energy dispersive scanning transmission electron microscopy was carried out using a FEI Talos F200X STEM operating at 200 kV. To test for differences in fresh vs spent catalyst surface chemistry, temperature programmed reduction (TPR) was performed using a Micromeritics AutoChem II 2920 unit. Prior to TPR analysis, 35 mg of catalyst was pretreated to 550 °C under He/O_2 gas mixture for 30 min. After which, the TPR was carried out to 600 °C under H_2/Ar atmosphere at a gas flow rate of 50 ml min^{-1}, temperature ramp of 10 °C min^{-1}, and thermal conductivity detection (TCD).

2.4. Hydrothermal catalyst activity

Mono- and bimetal catalyst activity was evaluated for hydrothermal conversion of oleic acid to stearic acid (hydrogenation, Eq. (1a)) and subsequent conversion to heptadecane (decarboxylation, Eq. (1b)) and possibly other hydrocarbon products. Hydrothermal batch reactions were performed in a stainless steel Swagelok microreactors (1.27 cm outer diameter × 10 cm length, 0.12 cm wall thickness) heated by submerging in a fluidized sand bath. Previous tests showed that the microreactors reach setpoint temperatures in <3 min (Li and Strathmann, 2019). Activity of the different catalysts were first compared at baseline conditions where 30 mg of catalyst was reacted with 100 mg of oleic acid and 20 mg methanol (as a source for *in situ* hydrogen production) in 1 m water at 350 °C for 5 h. Controls containing no catalyst were also performed at the same conditions. Activity of the most promising catalyst was further examined at a range of reaction conditions, including organic hydrogen source and concentration, temperature, and time. For comparison, reactions were also conducted with stearic (saturated fatty acid analogue) and linoleic acid (polyunsaturated fatty acid analogue) as the starting reactant. Reactions were quenched by removing reactors from the heated sand bath and submerging in a bath of water at room temperature. Once cooled, reactor contents were removed and washed three times with dichloromethane (DCM, 10 ml total) to extract residual fatty acid and conversion products. All reactions were carried out at least in duplicate.

Fatty acids and hydrocarbons were analyzed by gas chromatography using a flame ionization detector (GC-FID; Thermo Scientific TRACE 1310 equipped with an Agilent DB-Wax 30 $m \times 0.25$ mm × 25 μm capillary column). Hydrocarbon products were directly analyzed after injecting DCM extracts. For fatty acid analysis, samples were first subjected to a fatty acid methyl esterification (FAMES) procedure (Araujo et al., 2008) before GC-FID analysis. The injection and detection temperatures were 250 and 280 °C, respectively. Column temperature was increased from 50 to 200 °C at a ramp rate of 25 °C min^{-1} and then further to 230 °C at a ramp rate of 3 °C min^{-1}. High purity H_2 served was used as a carrier gas.

Oleic acid conversions were calculated in molar yield percentages to gage the activity and selectivity of respective catalysts. Eqs. (2-3) were used to determine such activity and are as follows:

$$Conversion\ (mol\%) = \left(1 - \frac{mol\ oleic\ acid\ final}{mol\ oleic\ acid\ initial}\right) \times\ 100 \tag{2}$$

$$Product\ Yield\ (mol\%) = \left(\frac{mol\ product}{mol\ initial\ oleic\ acid}\right) \times\ 100\% \tag{3}$$

3. Results & discussion

3.1. Oleic acid reactivity with mono- and bimetallic Ni and Cu catalysts

Fig. 1 shows results from initial experiments screening reactivity of oleic acid, a representative long-chain mono-unsaturated fatty acid, with mono-metal (Ni and Cu) and bimetal (Ni-Cu) ZrO_2-supported catalysts. ZrO_2 alone only led to minimal conversion of oleic acid to the corresponding saturated fatty acid, stearic acid, after 5 h of reaction. ZrO_2 co-precipitated with Cu, however, saw more than double the conversion of oleic acid and production of stearic acid. No catalysts saw heptadecane production in the absence of nickel (Fig. 1a, Table 1). These findings track with those found by Zhang et al. when employing Cu on ZrO_2 for hydrodeoxygenation of oleic acid with methanol as a hydrogen source. In comparison, complete conversion of oleic acid was observed during reactions with Ni/ZrO_2 and $Ni\text{-}Cu/ZrO_2$, with a mix of stearic acid and heptadecane products, the latter being the product of stearic acid decarboxylation. The GC-FID chromatograms (Fig. 2) showed minimal formation of other hydrocarbon cracking products, estimated to be <5% of product% yield. These products were relatively irrelevant for alkane production productivity and thus were not included in the final yields reported. It should be noted that, even when considering the cracking products, the quantified products don't lead to mass balance closure. This finding is not atypical for hydrothermal reactions, (Papageridis et al., 2020; Zhang et al., 2018c; Miao et al., 2016; Cai et al., 2022) particularly those conducted over nickel catalysts given its lack of controllability (Ananikov, 2015). For example, oleic acid is susceptible to aromatization under these conditions (Tian et al., 2017). Additionally, if acetic acid is generated via hydrocarboxylation of the methanol precursor, which has been shown to be promoted by

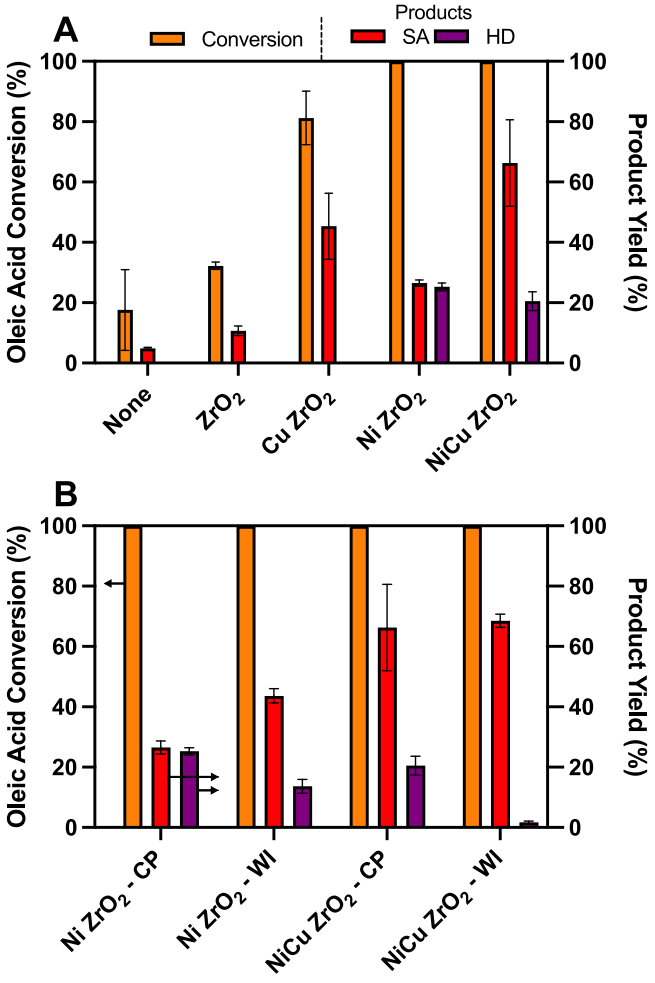

Fig. 1. Oleic acid conversion during hydrothermal reactions with Ni- and Cu-mono-metallic and bimetallic catalysts on ZrO_2 supports. (A) Oleic acid conversion (left axis) and yields for stearic acid and heptadecane products (right axis) over catalysts prepared by co-precipitation methods. (B) Comparison of Ni/ZrO_2 and $Ni\text{-}Cu/ZrO_2$ catalysts prepared by co-precipitation versus wet impregnation methods. Reaction conditions: 100 mg oleic acid, 20 mg methanol, 30 mg catalyst, 1000 mg water, 350 °C, t_{rxn} = 5 h.

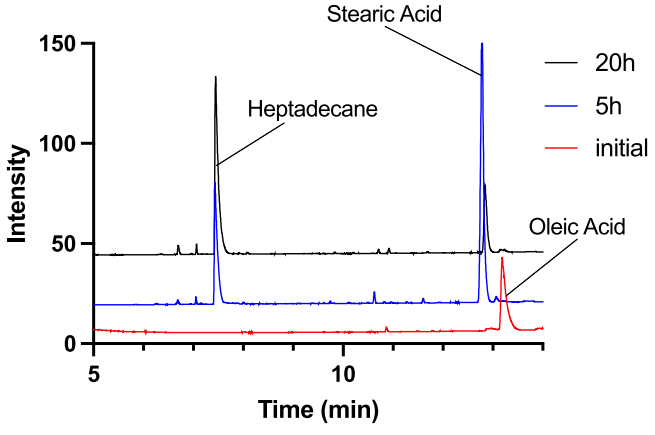

Fig. 2. GC-FID chromatogram showing oleic acid peak diminishing over time while stearic acid and heptadecane peak increase over time. Conditions are the same as Fig. 1.

ruthenium based catalysts, its presence can promote the peracid mechanism for the epoxidation of oleic acid (Qian et al., 2016; Jalil et al., 2019). Oleic acid epoxides can then polymerize to form polyesters and other long chain products with low vapor pressures making them difficult to detect by common analytical techniques (Japir et al., 2021; Borugadda and Dalai, 2018; Yeh et al., 2015). The presence of an unsaturated bond is necessary for these reactions, which is supported by the relatively higher mass balance achieved when starting with a saturated fatty acid (e.g., see Fig. 5). It is assumed that the products of these side reactions are consuming the remainder of the oleic acid, and no mass is being lost between reactor loading and product analysis. Surprisingly, heptadecane yields were slightly higher for the monometal Ni/ZrO_2 (25.3%) compared to the bimetallic (20.5%) catalyst. This finding contrasts with the recent report by Zhang and co-workers (Zhang et al., 2018a), where heptadecane yields were markedly higher for Cu-Ni/ZrO2 (32.2%) compared with Ni/ZrO_2 (22.7%) at the same reaction conditions used here and 3 h of reaction. The promotional reaction effects attributed to Cu in bimetallic catalysts are often recognized as electronic manipulation of the active metal catalyst via bimetal alloying (Kim et al., 2014). If metals are alloyed, their coordination state shifts, which is hypothesized to impact reactivity characteristics like intermediate adsorption time (Jin and Choi, 2019). XRD results in Fig. 3a suggest that Cu and Ni are alloyed. Therefore, alloying cannot be independently claimed as the key to reactive synergy. It is possible that the addition of copper interferes with this interaction, possibly intercepting the support and the nickel at their interface. In future discussion, we acknowledge the significance of support interactions with the active metal, justifying how this interception could inhibit nickel's activity. It should also be noted that the study by Zhang et al. yielded higher *in-situ* pressure generation due to a higher loading to reactor headspace ratio, which could have promoted activity. The requirement of Ni for high overall activity is consistent with the metal's documented behavior in hydrogenation applications (Ananikov, 2015; Wang et al., 2020; Li et al., 2022). However, the requirement for decarboxylation is less clear given the non-reductive nature of decarboxylation reactions. Vardon and co-workers (Vardon et al., 2014) also observed elevated rates of stearic acid decarboxylation by Pt/C and Pt-Re/C catalysts when applying a reducing $H_{2(g)}$ headspace compared to inert $N_{2(g)}$ headspace despite the non-reductive nature of the reaction mechanism. It was hypothesized that the reducing conditions served to maintain the active metals in their catalytic form.

Further tests supported the use of co-precipitation as an effective method for catalyst synthesis, as both the Ni and Ni-Cu catalysts prepared by alternative methods of wet impregnation of the ZrO_2 support proved to be less active for the decarboxylation step critical to heptadecane formation (Fig. 1b). The high reactivity of co-precipitated $Ni\text{-}Cu/ZrO_2$ has been attributed to increased nickel dispersion and metal-support contact, both initially due to nucleation rate differences of the two metals and long term due to stabilization effects by the bimetal (Liang et al., 2017; Elliott et al., 2006).

3.2. Catalyst characterization

Fig. 3 and Table 2 summarizes characteristics of the mono- and bimetallic catalysts, including Ni and Cu content from ICP-AES analysis. Catalysts were prepared with theoretical loadings of 15 wt% for each metal on the ZrO_2 support, with ICP-AES analysis showing some divergence from these values. Higher than expected values can be attributed to less than theoretical $ZrO_{2(s)}$ recovery from solution. Nonetheless, active metal contents in the most active co-precipitated formulations of Ni/ZrO_2 and $Ni\text{-}Cu/ZrO_2$ were close to the nominal values.

XRD analysis confirmed that all synthesized materials were tetragonal ZrO_2 (t-ZrO_2). These were used, in part, because commercial sources of ZrO_2 are typically the less active monoclinic form of ZrO_2 (Samson et al., 2014). The presence of a t-ZrO_2 phase is indicated by XRD diffraction peaks at 2θ of 30.2°, 50.4°, 50.6°, and 60.0° (full scan

Table 1
Reaction condition and product yield table.

Catalyst	Temperature (°C)	Time (h)	Fatty Acid	H_2 Source	Yield (%)		
					HD	SA	OA
ZrO_2	350	5	OA	Methanol	0.0 (±0)	10.7(±1.59)	80.0 (±1.19)
NiCu ZrO_2 - WI	350	5	OA	Methanol	1.7 (±0.44)	68.5 (±2.17)	non-detect
NiCu ZrO_2 - CP	350	5	OA	Methanol	20.5 (±3.11)	66.3 (±14.3)	non-detect
Cu ZrO_2 - CP	350	5	OA	Methanol	0.0 (±0)	41.1 (±4)	45.3 (±0)
Ni ZrO_2 - WI	350	5	OA	Methanol	13.7 (±2.39)	41.3 (±2.36)	non-detect
Ni ZrO_2 - CP	350	5	OA	Methanol	25.3 (±1.21)	26.5 (±2.17)	non-detect
Ni ZrO_2 - CP	200	5	OA	Methanol	0.0 (±0)	12.3 (±0.38)	61.0 (±6.0)
Ni ZrO_2 - CP	300	5	OA	Methanol	3.0 (±0.34))	59.8 (±5.97)	non-detect
Ni ZrO_2 - CP	325	5	OA	Methanol	13.4 (±1.10)	44.6 (±1.50)	non-detect
Ni ZrO_2 - CP	370	5	OA	Methanol	42.2 (±0)	16.7 (±.92)	1.1 (±.04)
Ni ZrO_2 - CP	350	2	OA	Methanol	7.5 (±1.07)	43.8 (±12.01)	non-detect
Ni ZrO_2 - CP	350	20	OA	Methanol	41.1 (±3.52)	16.11 (±3.79)	non-detect
Ni ZrO_2 - CP	350	30	OA	Methanol	51.5 (±6.88)	6.2 (±5.32)	non-detect
Ni ZrO_2 - CP	350	5	SA	Methanol	62.4 (±1.05)	5.0 (±.27)	–
Ni ZrO_2 - CP	350	5	LA	Methanol	9.81 (±1.84)	31.77 (±6.13)	non-detect
Ni ZrO_2 - CP	350	5	OA	Glycerol	8.3 (±1.72)	54.1 (±6.06)	non-detect
Ni ZrO_2 - CP	350	5	OA	Formic Acid	6.6 (±1.36)	41.3 (±2.24)	non-detect
Ni ZrO_2 - CP	350	5	OA	None	3.7 (±2.13)	43.4 (±1.80))	3.4 (±1.70)
Ni ZrO_2 – CP[a]	350	5	OA	Methanol	12.2 (±0)	26.5 (±0)	non-detect
Ni ZrO_2 – CP[b]	350	5	OA	Methanol	10.4 (±0)	67.61 (±2.91)	non-detect

[a] Catalyst recovered after 20 h experiment and re-ran
[b] catalyst ran after 20 h hydrothermal treatment at 350 °C, *resulting linoleic acid. OA: Oleic acid, SA: Stearic Acid, LA: Linoleic acid, HD: Heptadecane.

Table 2
Catalyst compositional and morphological characterizations.

Catalyst	Metal Content (wt%)[a]	
	Ni	Cu
Ni-Cu/ZrO_2 (WI)	8.40	12.70
Ni-Cu/ZrO_2 (CP)	14.69	14.90
Ni/ZrO_2 (WI)	23.35	0.16
Ni/ZrO_2 (CP)	15.49	0.14
Cu/ZrO_2 (CP)	0.44	24.08
ZrO_2	0.18	0.03
Spent Aq	0.065	0.00
Spent Ni ZrO_2	17.65	0.00

Measured by.
[a] ICP-MS.

XRD data provided in Fig. S1 in Supplementary Materials). For m-ZrO2, peaks would have been observed at $2\theta = 28.7^\circ$ and 34.2°. Additionally, XRD showed peaks at 43.9°, 50.6°, and 74.9°, which are representative of nickel and copper hybridized face-centered-cubic lattice peaks at signature (001), (200), and (220) planes respectively. The lack of a distinguished Ni peak at 45° in Fig. 3a-2 is either due to high dispersion leading to low diffractive definition, or peak overlay by ZrO_2 at 45.5° (Fig. 3a-4). Regardless, the peak shift to a centralized 44° position in Fig. 3a-3 indicates a hybrid diffraction between Ni and Cu which suggests metal-metal interaction. The orientation of such peaks are slightly offset between what would normally be characteristic locations of these lattice dimensions for both nickel and copper, possibly suggesting an alloyed bimetal structure.

Dispersion of Ni and Cu on the synthesized materials was variable as shown in the STEM-EDS images provided in Fig. 3b–e. The co-precipitated Ni-Cu bimetallic catalyst shows finite nickel agglomerates embedded in the support matrix with copper more evenly dispersed. In comparison, wet impregnation of the Ni and Cu salts leads to larger agglomerated clusters around the ZrO_2 support. These findings are consistent with reports by Zhang et al. that co-precipitation of Ni (and Cu in the case of bimetallic formulation) with Zr maximizes active metal-support interfaces that may be important for hydrothermal catalytic activity with oleic acid (Zhang et al., 2020). Fig. 3d, e show STEM-EDS and SEM of the fresh Ni/ZrO_2 (CP) catalyst synthesized via co-precipitation. SEM shows the morphology to be clumpy with slight geometric features and looks of deposits/growth on a larger support (Fig. 3e).

Differences in reactivity observed with oleic acid (Fig. 1) go beyond elemental composition. Ni/ZrO_2 prepared by co-precipitation showed higher heptadecane yields than the catalyst prepared by wet impregnation of Ni onto ZrO_2, despite the latter formulation having significantly higher Ni content. The low activity of the bimetallic catalyst prepared by wet impregnation methods may result from incongruent deposition wherein Cu overlays Ni, limiting interactions with fatty acids or the hydrogen donor. Bimetal deposition is highly sensitive to synthesis conditions and slight deviations of metal collocation has shown to make large differences in the adsorptive behavior of the catalyst (Zhao et al., 2016; Yang and Cheng, 2014). During co-precipitation, the concerted nucleation of all metals promotes mixed metal deposition, which can prevent active site blockage (Tang et al., 2018). Additionally, coprecipitation of the support in the presence of simultaneously nucleating metals can also promote the formation of a higher concentration of oxygen vacancies in the support ZrO_2, since the introduction of structural impurities can induce reverse oxygen spillover. Such vacancies may strengthen support-metal interactions and stabilize the support by lowering the dielectric constant as a result of lattice distortion around the vacancy (Samson et al., 2014; Chen et al., 2014; Gao et al., 2011).

3.3. Reactivity of Ni/ZrO_2

While these findings support earlier reports by Zhang and co-workers, the higher than anticipated reactivity observed for co-precipitated Ni/ZrO_2 calls for a more in-depth examination of the material's hydrothermal reactivity with oleic acid and related fatty acids. Fig. 4 shows the effects of reaction temperature (Fig. 4a), reaction time (Fig. 4b), and catalyst loading (Fig. 4c) on oleic acid conversion and yields of heptadecane and stearic acid products. Complete conversion of oleic acid with Ni/ZrO_2 within 5 h was observed at all temperatures >200 °C, but decarboxylation to produce heptadecane was not appreciable until temperatures reached 325 °C (Fig. 4a), reaching a maximum of 42% at 370 °C. Interestingly, side products decreasing stearic acid and heptadecane yields were already significant at a temperature of 200 °C, but only increased slightly at higher temperatures reflecting competition among parallel pathways for oleic acid conversion.

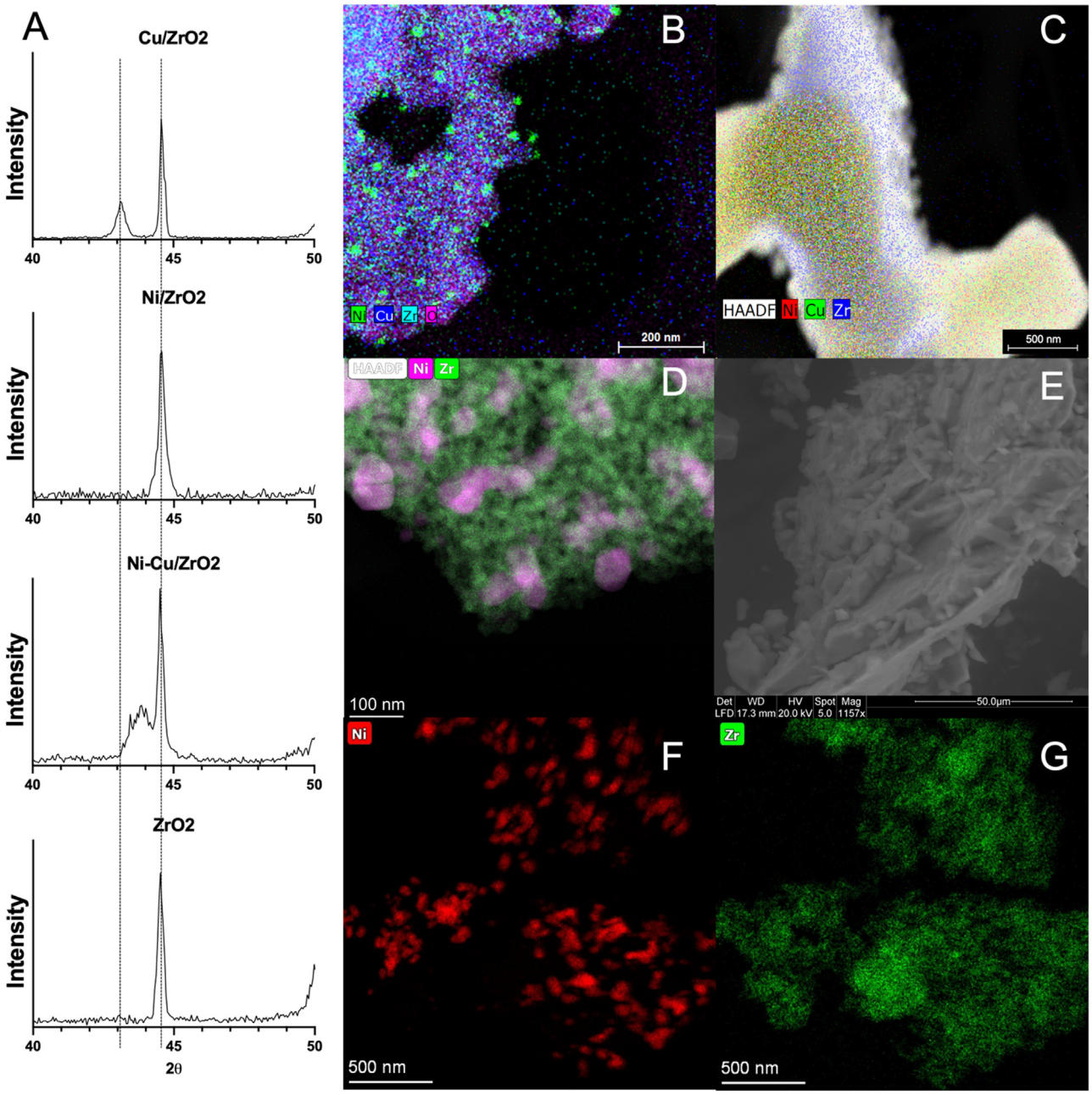

Fig. 3. X-ray diffraction, TEM-EDS, and SEM catalyst characterization. (A) Closeup XRD patterns of (top to bottom) co-precipitated Cu/ZrO_2, Ni/ZrO_2, $Ni\text{-}Cu/ZrO_2$, and ZrO_2. STEM EDS mapping of (B) $Ni\text{-}Cu/ZrO_2$ (CP), (C) $Ni\text{-}Cu/ZrO_2$ (WI), (D) Ni/ZrO_2 (CP – Fresh), (F-G) Ni/ZrO_2 (CP-Spent). (E) SEM image of Ni/ZrO_2(CP).

A reaction temperature of 350 ˚C, intermediate between conditions where heptadecane production was observed, was used when examining other system variables. Complete conversion of oleic acid at this temperature was observed within 2 h, yielding principally stearic acid, but longer reaction times were required to further convert the saturated fatty acid to heptadecane (Fig. 4b). Further increases in heptadecane yield were limited after 20 h. Dosing additional methanol at t = 20 h also had limited effect on further conversion, so availability of excess hydrogen was not believed to be responsible for the stalled conversion. This is more likely the result of hydrothermal water-induced catalyst deactivation during the first 20 h of reaction. This would be consistent with previous reports (Wang et al., 2014; Elliott, 2008; Champon et al., 2020). Reasons for reduced activity are explored in Section 3.6.

The yields shown in Fig. 4a and Table 1 should be contextualized in the literature of materials used for hydrothermal deoxygenation. Noble metals are the most prominent for these reactions and their higher yields are not unprecedented. Reports by Fu and coworkers (Fu et al., 2010, 2011) evaluate platinum and palladium on carbon for hydrothermal deoxygenation of fatty acids. At a reaction temperature of 330 ˚C, they observed a 9.3% yield of heptadecane over Pt/C from oleic acid after 1.5 h with no added hydrogen source. Interestingly, when starting with palmitic acid they observed a 55% yield for the decarboxylation product, pentadecane, after just 1 h. When starting with Pd/C, this yield dropped slightly to 50% pentadecane. Additionally, Vardon et al. observed a 37% heptadecane yield after 9 h of reacting a Pt-Re/C bimetal catalyst at 330 ˚C with oleic acid using glycerol as a hydrogen donor (Vardon et al., 2014). Ni/ZrO_2 has also been explored for stearic acid hydrothermal deoxygenation by Miao et al. in 2018, which yielded 37% heptadecane after 9 h at 330 ˚C in the absence of an external H_2 source (Miao et al., 2018). This agrees reasonably well with the yield

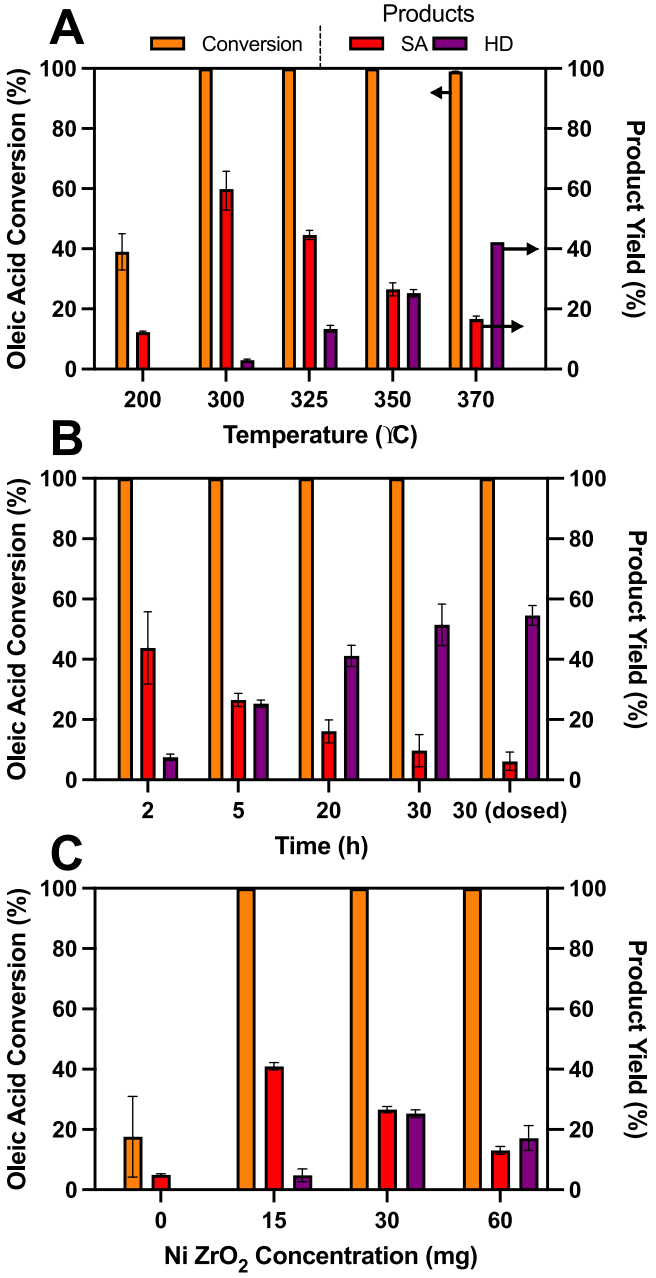

Fig. 4. Oleic acid conversion (left axis) and yields for stearic acid and heptadecane products (right axis) over Ni ZrO_2 as a function of (A) reaction temperature, (B) reaction time, and (C) catalyst loading. Reaction conditions the same as Fig. 1, except the parameter being varied. For panel (A), data point 30 (dosed), reactor was opened and re-spiked with 20 mg methanol at t = 20 h before reacting for an additional 10 h.

we observed after reacting stearic acid for 5 h at 350 °C, albeit in the presence of methanol as a H_2 source (Table 1). In 2021, Zeng at al. was able to achieve 60% heptadecane yield from stearic acid using Co_3O_4 nanoparticles and a carbon matrix shell, underscoring the possibilities that advanced catalyst design can have for the future of non-noble metal deoxygenation catalysis (Zeng et al., 2022).

In the absence of a catalyst, around 18% of oleic acid was converted to other products, 27% was converted to stearic acid and none of it was converted to heptadecane (Fig. 4c). However, when 15 mg of the catalyst was loaded, rather than the typical 30 mg, the heptadecane yield dropped about 80% and the stearic acid yield almost doubled from 26% to 40%. Counterintuitively, when doubling the catalyst weight from

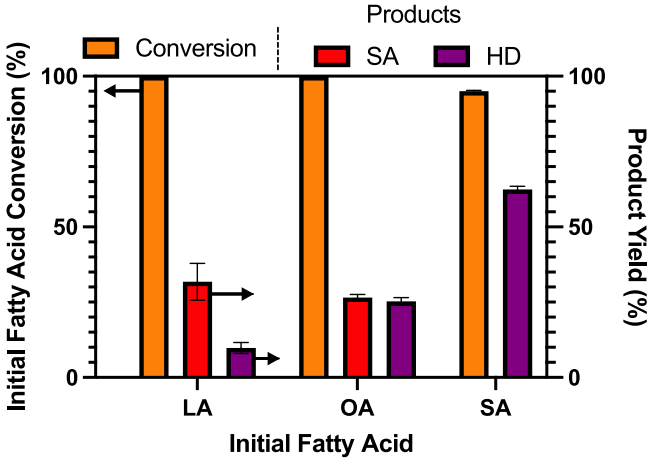

Fig. 5. Conversion of linoleic (LA), oleic (OA), and stearic (SA) acid (left axis) and yields for oleic acid, stearic acid and heptadecane (HD) products (right axis) over Ni/ZrO_2. Reaction conditions were the same as Fig. 1.

30 mg to 60 mg, heptadecane and stearic acid yields dropped to 17% and 12%, respectively, with complete oleic acid conversion retained. This optimum concentration suggests parallel pathways (e.g. polymerization, saponification, isomerization, etc.) are promoted by Ni ZrO_2 and such are able to overcome decarboxylation in the presence of excess material. It should be noted that products produced from these pathways were not identified or quantified, however, there is a possibility that aromatics make up a portion of these products (Zhang et al., 2018b). Though these products have been found to be minimal in aqueous solvent systems (Tian et al., 2017), if produced they could be valorized for their high energy density and low smoke point heavily valued for diesel and jet fuel.

3.4. Comparing the fatty acid degree of saturation

Hydrothermal conversion experiments were also performed for the corresponding saturated fatty acid, stearic acid, and polyunsaturated fatty acid, linoleic acid, both with and without Ni/ZrO_2. Results shown in Fig. 5 show that heptadecane production over the 5 h increases with increasing degree of initial fatty acid saturation. The only fatty acid that didn't see full conversion was stearic acid, further supporting that hydrogenation (Eq. (1a)) is not the rate limiting step in the production of heptadecane. It should be noted that, since full hydrogenation occurred in each reaction, no residual linoleic or oleic acid was detected, therefore they are not listed as products in Fig. 5. Cumulative heptadecane product yields also decreased with increasing degree of saturation, suggesting that the double bond(s) promote the rate of parallel side reactions that will deviate reactants from the desired deoxygenation pathway.

3.5. Hydrogen donor

Following from earlier work (Zhang et al., 2018a), methanol was added to reactor solutions to serve as a source for *in situ* hydrogen production in place of pressurized H_2 gas addition. H_2 is not only necessary for the saturation of oleic acid, but also the continuous reduction of the metal into its active metallic state. In hydrothermal water, methanol and other low molecular weight organic co-constituents can undergo aqueous phase reformation (APR) (Stekrova et al., 2018; Coronado et al., 2017). For example, each mole of methanol can react to form up to 3 mol equivalents of H_2 with suitable catalyst and temperature (Eq. 4): (Coronado et al., 2017)

$$CH_3OH\ (methanol) + H_2O \rightarrow 3H_2 + CO_2 \quad (4)$$

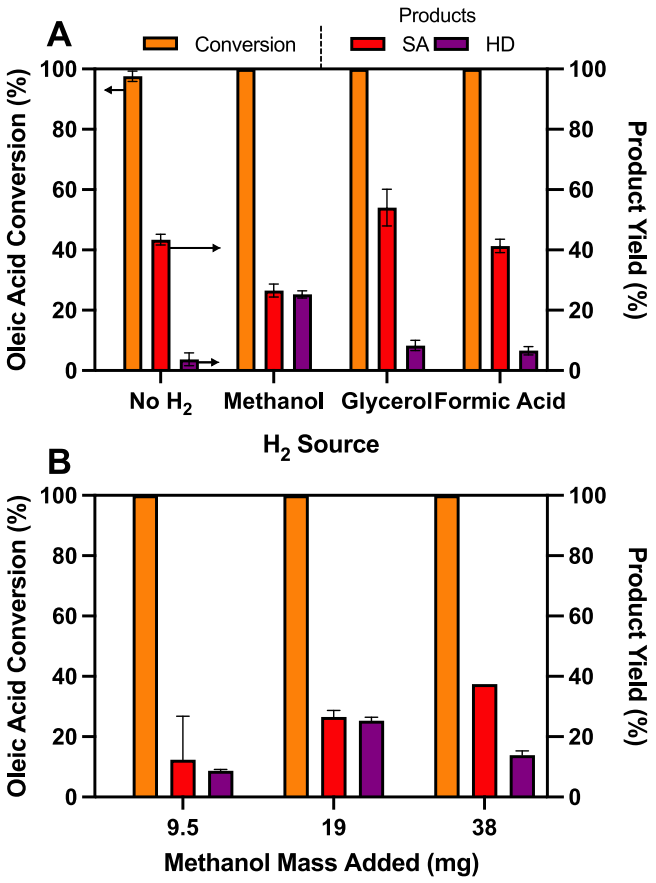

Fig. 6. Influence of (A) *in situ* hydrogen source and (B) methanol loading on conversion of oleic acid and selectivity to stearic acid and heptadecane products. For (A), added hydrogen sources were 20 mg methanol, 20 mg glycerol, or 81.0 mg formic acid. The initial values were varied to produce theoretical H_2 yields of 5 mol of H_2 per mole of oleic acid added to the reactor. Other reactions conditions were the same as Fig. 1.

In comparison, each mole of glycerol ($C_3H_8O_3$) and formic acid (CH_2O_2) can react to form up to 7 mol and 1 mol of H_2, respectively (Eqs. (5-6)):

$$C_3H_8O_3\ (glycerol) + 3H_2O \rightarrow 7H_2 + 3CO_2 \quad (5)$$

$$CH_2O_2\ (formic\ acid) \rightarrow H_2 + CO_2 \quad (6)$$

Fig. 6a shows the effects of adding different hydrogen donor sources in oleic acid conversion by Ni/ZrO_2. Added concentrations of individual hydrogen donors were varied according to source to keep total theoretical H_2 production constant. Pressure variations resulting from differing hydrogen source loadings were taken to be negligible. Results showed that oleic acid conversion was dependent on hydrogen donor source, with heptadecane yields being greatest for methanol in comparison to glycerol and formic acid, despite the same theoretical hydrogen production potential. These discrepancies in decarboxylation potential can be related to the structures of the hydrogen donors. It has been shown that the binding of acidic functional groups, like that in formic acid, to the basic sites of amphoteric ZrO_2 impedes catalytic transfer hydrogenation (CTH) responsible for hydrogenation and cyclization of butyl levulinate to valerolactone (Chia and Dumesic, 2011). Similar blockage could be inhibiting H_2 donation or blocking sites necessary for reactant adsorption for reaction. Polyalcohols including sugars undergo aqueous phase reforming for H_2 production similarly to methanol. However, methanol has been shown to have a greater selectivity for hydrogen when reformed over nickel (Coronado et al., 2016). Additionally, the methanol and water solvent mixture has been shown to have synergistic effects for biomass liquification, which also contains hydrogenation (Zhang et al., 2019; Zhao et al., 2020).

Fig. 6b shows the effect of varying methanol concentration initially added to the reactor. In the absence of an external hydrogen source, oleic acid was still able to be hydrogenated, indicating the ability of Ni ZrO_2 to promote the water gas shift reaction and produce H_2 *in situ*. While the catalyst fully converted oleic acid at all conditions, heptadecane yield and overall product yield was lower when the methanol concentration was cut in half compared to the baseline concentration. More surprisingly, though, we also found that heptadecane yields dropped when higher methanol concentrations were used despite higher stearic acid yields. This suggests that formation of other products of APR, e.g., dissolved carbonate species, may act to inhibit stearic acid decarboxylation if present in too high of concentration. One such product could be CO, formed form either decarbonylation of the fatty acid or the reverse water gas shift reaction mentioned previously. CO has been shown to block nickel active sites, which would slow the production of heptadecane (Loe et al., 2019; Jackson et al., 1998). It is possible that some H_2 donor precursors such as formic acid or glycerol could also promote the production of CO, which might limit decarboxylation efficiency. Future work is recommended to measure H_2 and CO generation directly during reactions, which was precluded by the micro-reactors used in the present study.

3.6. Catalyst deactivation and recycling

Finally, experiments were conducted to assess deactivation and potential regeneration of Ni/ZrO_2 catalysts. It was already discussed that reactions appeared to stall after 20 h of reaction initiated with oleic acid, with further decarboxylation of stearic acid to heptadecane being limited between 20 and 30 h of reaction. Addition of a second spike of methanol had little effect, indicating that the stalled activity was not the result of limiting hydrogen supply (which we estimated to be in significant excess of hydrogenation requirements to begin with). These findings are consistent with previous reports of deactivation of Ni-based catalysts, where loss in activity is often attributed to corrosion, sintering, or leaching of the active metal, or surface coking of organic products (Crawford et al., 2020; Miao et al., 2016; Cheng et al., 2021; Champon et al., 2020). Analysis of dissolved Ni after the initial 20 h of reaction (Table 2) indicated minimal leaching, so other deactivation mechanisms were suspected. A separate recycling experiment compared oleic acid conversion using Ni/ZrO_2 which had already reacted for 20 h with oleic acid compared to virgin catalyst. Partial deactivation was observed, where yields for heptadecane were 52% lower for the used catalyst than virgin catalyst (Fig. 7). Additional experiments showed that the catalyst deactivation occurs regardless of whether or not oleic acid and methanol are introduced with the catalyst to the hydrothermal media during the 20 h prior to initiating the reaction.

Catalyst exposed to hydrothermal conditions for 20 h before introducing oleic acid and methanol was similarly deactivated (Fig. 7), excluding potential active site coverage by deposited organic species as the primary mode of deactivation. Catalyst pre-exposed to 20 h of hydrothermal conditions was also subjected to reactivation through recalcination and furnace reduction as described in the initial catalyst synthesis procedure. Results showed no recovered activity for heptadecane production (Fig. 7), suggesting that sintering may be responsible for the observed deactivation. The increase in the temperature of reduction as seen in H_2-TPR data (Fig. 8) is observed after catalyst deactivation, increasing from 276 °C to 313 °C after undergoing 20 h reaction. This increase indicates a less H_2-reactive form of Ni after extended exposure to the hydrothermal reaction environment. This may result from loss of active metal / support interaction upon hydrothermal treatment. Further, the shoulder peak observed in the fresh catalyst indicates inner-support nickel particles which have maximized support interface, often responsible for greater activity (Roh et al., 2002;

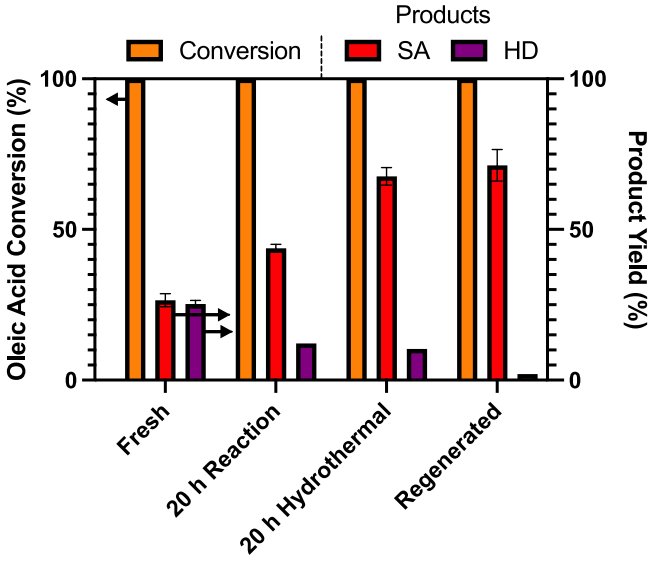

Fig. 7. Activity of virgin Ni/ZrO_2 in comparison with catalyst recycle following 20 h reaction, following 20 h pure hydrothermal treatment, and following re-exposure of the 20 h deactivated catalyst to calcination and $H_{2(g)}$ reactivation. Reaction conditions were the same as Fig. 1.

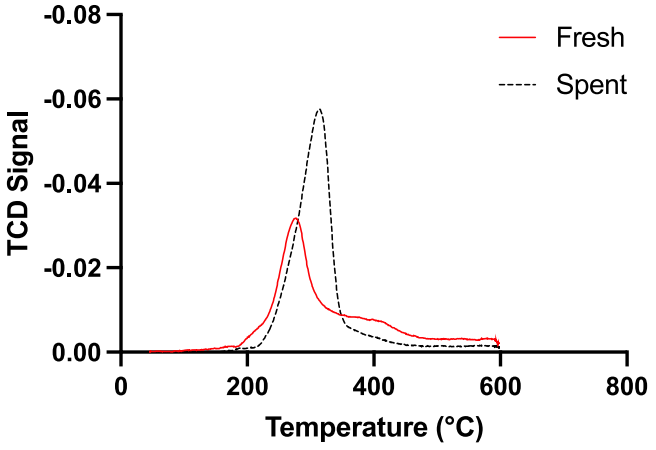

Fig. 8. H_2-temperature programmed reduction of "fresh" (red) and "20 h hydrothermal" spent (black) Ni/ZrO_2. Spent catalyst undergone 20 h reaction with reaction conditions mentioned in Fig. 1.

Zhang et al., 2020). These results support that metal migration and sintering from the bulk to the surface occurs under hydrothermal conditions. Metal migration also displaces metals from their initial support deposition chemistry, disrupting the electronic effects offered by this interaction and leading to lower reducibility of the nickel (Colorado School of Mines, 2023). Catalyst activity recovery post-sintering has not yet been formalized in literature. Therefore, it should be prioritized in future work to synthesize catalysts in a way which limits or slows this morphological transformation in the hydrothermal reaction environment. Bimetals have been shown to prevent metal migration. However, copper did not prove useful for this purpose in similar deactivation experiments conducted here. Another option would be physical anchoring of the metals in the support matrix through ligands (Jenkins and Medlin, 2021), complex organic framework caging (Zhao et al., 2018), or surface locking through synthesis modification (Yang et al., 2019). Successful material development to circumvent this deactivation could further the competitiveness of this earth abundant catalyst against its noble metal counterparts.

4. Conclusions

Co-precipitated Ni on tetragonal ZrO_2 proved to produce the most efficient catalyst for decarboxylation of C18 fatty acids to heptadecane under subcritical hydrothermal conditions (300 – 370 °C). Non noble active metals were chosen for evaluation due to their price point relative to other commonly used platinum group transition metals which can cost over 99% more (Daily Metal Price: Free Metal Price Tables and Charts, 2023, BASF, 2023). Influence of copper as a non-noble bimetal on this reaction was null, contradicting recent reports. Methanol outperformed other organic liquid hydrogen sources. Catalyst and hydrogen donor loading were found to have an optimizable concentrations to encourage the reaction towards decarboxylation and away from fatty acid consuming parallel reactions. Greater heptadecane selectivity was observed when stearic acid was used as the starting reactant, emphasizing that the undesired parallel reaction pathways are more significant for the unsaturated fatty acid than saturated fatty acids. Deoxygenation over the active mono-metal catalyst scaled with temperature and reaction time up until the deactivation threshold, at which point metal sintering appears to deactivate the material. These specifications can inform optimal use of Ni ZrO_2 for deoxygenation of fatty acids to liquid alkanes, however, more information regarding preventative deactivation synthesis is necessary to further advance these materials as a reliable alternative to their noble metal counterparts.

Funding statement

Financial support for this work was provided by the National Science Foundation (NSF) through the NSF Engineering through the NSF Engineering Research Center for Reinventing the Nation's Urban Water Infrastructure (ReNUWIt; EEC-1028968) and NSF award CBET-1804513.

Declaration of Competing Interest

The authors declare that they have no known competing financial interests or personal relationships that could have appeared to influence the work reported in this paper.

Data availability

Data will be made available on request.

Acknowledgements

Financial support for this work was provided by the National Science Foundation (NSF) through the NSF Engineering through the NSF Engineering Research Center for Reinventing the Nation's Urban Water Infrastructure (ReNUWIt; EEC-1028968) and NSF award CBET-1804513. Moises Carreon, Praveen Kumar, Melodie Chen-Glasser, Ryan Richards, Galen Dennis and Matthew Posewitz (CSM) are acknowledged for assistance with analysis and materials characterization.

Supplementary materials

Supplementary material associated with this article can be found, in the online version, at doi:10.1016/j.hazadv.2023.100273.

References

Al-Muhtaseb, A.H., Osman, A.I., Murphin Kumar, P.S., Jamil, F., Al-Haj, L., Al Nabhani, A., Kyaw, H.H., Myint, M.T.Z., Mehta, N., Rooney, D.W., 2021. Circular economy approach of enhanced bifunctional catalytic system of CaO/CeO_2 for biodiesel production from waste loquat seed oil with life cycle assessment study. Energy Convers. Manag. 236, 114040. doi:10.1016/j.enconman.2021.114040.

Amatayakul, W., Ramnäs, O., 2001. Life cycle assessment of a catalytic converter for passenger cars. J. Clean. Prod. 9 (5), 395–403. doi:10.1016/S0959-6526(00)00082-2.

Ananikov, V.P., 2015. Nickel: the "spirited horse" of transition metal catalysis. ACS Catal. 5 (3), 1964–1971. doi:10.1021/acscatal.5b00072.

Araujo, P., Nguyen, T.T., Frøyland, L., Wang, J., Kang, J.X., 2008. Evaluation of a rapid method for the quantitative analysis of fatty acids in various matrices. J. Chromatogr. A 1212 (1), 106–113. doi:10.1016/j.chroma.2008.10.006.

Awogbemi, O., Kallon, D.V.V., Aigbodion, V.S., Panda, S., 2021. Advances in biotechnological applications of waste cooking oil. Case Stud. Chem. Environ. Eng. 4, 100158. doi:10.1016/j.cscee.2021.100158.

BASF, 2023. Engelhard Industrial Bullion (EIB) Prices. BASF. https://apps.catalysts.basf.com/apps/eibprices/mp/.

Borugadda, V.B., Dalai, A.K., 2018. *In-situ* synthesis and characterization of biodegradable estolides via epoxidation from canola biodiesel. Lubricants 6 (4), 94. doi:10.3390/lubricants6040094.

Boualouache, A., Boucenna, A., 2020. Mechanistic details of methane dry reforming on copper-nickel bimetallic surfaces. Chem. Phys. Lett. 739, 136995. doi:10.1016/j.cplett.2019.136995.

Brownley, J., 2023. Sustainable Aviation Fuel Act.

H Burnett, J.W., Sun, Z., Li, J., Wang, X., Wang, X, 2021. Comparative life cycle assessment of NAD(P)H regeneration technologies. Green Chem. 23 (18), 7162–7169. doi:10.1039/D1GC02349G.

Cai, X., Zhang, Z., Ye, Y., Wang, D., Li, S., Wang, D., Zheng, Z., 2022. Conversion of higher fatty acids or higher fatty acid esters to long-chain alkanes by acid added metal catalyst under mild hydrothermal conditions. Biomass Bioenergy 156, 106328. doi:10.1016/j.biombioe.2021.106328.

Champon, I., Bengaouer, A., Chaise, A., Thomas, S., Roger, A.C., 2020. Modelling the sintering of nickel particles supported on γ-alumina under hydrothermal conditions. Catalysts 10 (12), 1477. doi:10.3390/catal10121477.

Chen, C., Ruan, C., Zhan, Y., Lin, X., Zheng, Q., Wei, K., 2014. The significant role of oxygen vacancy in Cu/ZrO_2 catalyst for enhancing water–gas-shift performance. Int. J. Hydrog. Energy 39 (1), 317–324. doi:10.1016/j.ijhydene.2013.10.074.

Cheng, F., Tompsett, G.A., Alvarez, D.V.F., Romo, C.I., McKenna, A.M., Niles, S.F., Nelson, R.K., Reddy, C.M., Granados-Fócil, S., Paulsen, A.D., Zhang, R., Timko, M.T., 2021. Metal oxide supported ni-impregnated bifunctional catalysts for controlling char formation and maximizing energy recovery during catalytic hydrothermal liquefaction of food waste. Sustain. Energy Fuels 5 (4), 941–955. doi:10.1039/D0SE01662D.

Chia, M., Dumesic, J.A., 2011. Liquid-phase catalytic transfer hydrogenation and cyclization of levulinic acid and its esters to γ-valerolactone over metal oxide catalysts. Chem. Commun. 47 (44), 12233–12235. doi:10.1039/C1CC14748J.

Mile, B., Stirling, D., Zammitt, M., Lovell, A., Webb, M. TPR Studies of the Effects of Preparation Conditions on Supported Nickel Catalysts. J. Mol. Catal. 1990, 62, 179–198. doi:10.1016/0304-5102(90)85212-Z.

Coronado, I., Stekrova, M., Reinikainen, M., Simell, P., Lefferts, L., Lehtonen, J., 2016. A review of catalytic aqueous-phase reforming of oxygenated hydrocarbons derived from biorefinery water fractions. Int. J. Hydrog. Energy 41 (26), 11003–11032. doi:10.1016/j.ijhydene.2016.05.032.

Coronado, I., Stekrova, M., García Moreno, L., Reinikainen, M., Simell, P., Karinen, R., Lehtonen, J., 2017. Aqueous-phase reforming of methanol over nickel-based catalysts for hydrogen production. Biomass Bioenergy 106, 29–37. doi:10.1016/j.biombioe.2017.08.018.

Crawford, J.M., Zaccarine, S.F., Kovach, N.C., Smoljan, C.S., Lucero, J., Trewyn, B.G., Pylypenko, S., Carreon, M.A., 2020. Decarboxylation of stearic acid over Ni/MOR catalysts. J. Chem. Technol. Biotechnol. 95 (1), 102–110. doi:10.1002/jctb.6211.

Daily Metal Price: Free Metal Price Tables and Charts. https://www.dailymetalprice.com/ (accessed 2023-03-06).

Dey, P., Ray, S., 2020. Comparative analysis of waste vegetable oil versus transesterified waste vegetable oil in diesel blend as alternative fuels for compression ignition engine. Clean. Technol. Environ. Policy 22 (7), 1517–1530. doi:10.1007/s10098-020-01892-1.

Elliott, D.C., Hart, T.R., Neuenschwander, G.G., 2006. Chemical processing in high-pressure aqueous environments. 8. Improved catalysts for hydrothermal gasification. Ind. Eng. Chem. Res. 45 (11), 3776–3781. doi:10.1021/ie060031o.

Elliott, D.C., 2008. Catalytic hydrothermal gasification of biomass. Biofuels Bioprod. Biorefining 2 (3), 254–265. doi:10.1002/bbb.74.

Freitas, I.C., Manfro, R.L., Souza, M.M.V.M., 2018. Hydrogenolysis of glycerol to propylene glycol in continuous system without hydrogen addition over Cu-Ni catalysts. Appl. Catal. B Environ. 220, 31–41. doi:10.1016/j.apcatb.2017.08.030.

Fu, J., Lu, X., Savage, P.E., 2010. Catalytic hydrothermal deoxygenation of palmitic acid. Energy Environ. Sci. 3 (3), 311–317. doi:10.1039/B923198F.

Fu, J., Lu, X., Savage, P.E., 2011. Hydrothermal decarboxylation and hydrogenation of fatty acids over Pt/C. ChemSusChem 4 (4), 481–486. doi:10.1002/cssc.201000370.

Gan, L.Y., Tian, R.Y., Yang, X.B., Lu, H.D., Zhao, Y.J., 2012. Catalytic reactivity of CuNi alloys toward H_2O and CO dissociation for an efficient water–gas shift: a DFT study. J. Phys. Chem. C 116 (1), 745–752. doi:10.1021/jp208119x.

Gao, D., Liu, L., Liang, H., Wu, W.M., 2011. Aerobic granular sludge: characterization, mechanism of granulation and application to wastewater treatment. Crit. Rev. Biotechnol. 31 (2), 137–152. doi:10.3109/07388551.2010.497961.

Jackson, S.D., Hussain, N., Munro, S., 1998. High-temperature adsorption of carbon monoxide and hydrocarbon gases over nickel and platinum catalysts. J. Chem. Soc. Faraday Trans. 94 (7), 955–961. doi:10.1039/A708074C.

Jalil, M.J., Yamin, A.F.M., Zaini, M.S.M., Ariff, M.A.M., Chang, S.H., Morad, N., Hadi, A., 2019. Synthesis of epoxidized oleic acid- based palm oil by peracid mechanism. IOP Conf. Ser. Mater. Sci. Eng. 551 (1), 012120. doi:10.1088/1757-899X/551/1/012120.

Japir, A.A.W.M.M., Salih, N., Salimon, J., 2021. Synthesis and characterization of biodegradable palm palmitic acid based bioplastic. Turk. J. Chem. 45, 585–599. doi:10.3906/kim-2011-31.

Jenkins, A.H., Medlin, J.W., 2021. Controlling heterogeneous catalysis with organic monolayers on metal oxides. Acc. Chem. Res. 54 (21), 4080–4090. doi:10.1021/acs.accounts.1c00469.

Jin, M., Choi, M., 2019. Hydrothermal deoxygenation of triglycerides over carbon-supported bimetallic PtRe catalysts without an external hydrogen source. Mol. Catal. 474, 110419. doi:10.1016/j.mcat.2019.110419.

Joshi, S.S., Zodge, A.D., Pandare, K.V., Kulkarni, B.D., 2014. Efficient conversion of cellulose to levulinic acid by hydrothermal treatment using zirconium dioxide as a recyclable solid acid catalyst. Ind. Eng. Chem. Res. 53 (49), 18796–18805. doi:10.1021/ie5011838.

Kim, D., Resasco, J., Yu, Y., Asiri, A.M., Yang, P., 2014. Synergistic geometric and electronic effects for electrochemical reduction of carbon dioxide using gold–copper bimetallic nanoparticles. Nat. Commun. 5 (1), 4948. doi:10.1038/ncomms5948.

Kumar, R., Strezov, V., Lovell, E., Kan, T., Weldekidan, H., He, J., Dastjerdi, B., Scott, J., 2019. Bio-oil upgrading with catalytic pyrolysis of biomass using copper/zeolite-nickel/zeolite and copper-nickel/zeolite catalysts. Bioresour. Technol. 279, 404–409. doi:10.1016/j.biortech.2019.01.067.

Li, Y., Strathmann, J.T., 2019. Kinetics and mechanism for hydrothermal conversion of polyhydroxybutyrate (PHB) for wastewater valorization. Green Chem. 21 (20), 5586–5597. doi:10.1039/C9GC02507C.

Li, B., Chen, J., Liu, D., Gridnev, I.D., Zhang, W., 2022. Nickel-catalysed asymmetric hydrogenation of oximes. Nat. Chem. 14 (8), 920–927. doi:10.1038/s41557-022-00971-8.

Liang, T., Wang, Y., Chen, M., Yang, Z., Liu, S., Zhou, Z., Li, X., 2017. Steam reforming of phenol-ethanol to produce hydrogen over bimetallic NiCu catalysts supported on sepiolite. Int. J. Hydrog. Energy 42 (47), 28233–28246. doi:10.1016/j.ijhydene.2017.09.134.

Lizhi, H., Toyoda, K., Ihara, I., 2008. Dielectric properties of edible oils and fatty acids as a function of frequency, temperature, moisture and composition. J. Food Eng. 88 (2), 151–158. doi:10.1016/j.jfoodeng.2007.12.035.

Loe, R., Lavoignat, Y., Maier, M., Abdallah, M., Morgan, T., Qian, D., Pace, R., Santillan-Jimenez, E., Crocker, M., 2019. Continuous catalytic deoxygenation of waste free fatty acid-based feeds to fuel-like hydrocarbons over a supported Ni-Cu catalyst. Catalysts 9 (2), 123. doi:10.3390/catal9020123.

Luo, J., Monai, M., Wang, C., Lee, J.D., Duchoň, T., Dvořák, F., Matolín, V., Murray, C.B., Fornasiero, P., Gorte, R.J., 2017. Unraveling the surface state and composition of highly selective nanocrystalline Ni–Cu alloy catalysts for hydrodeoxygenation of HMF. Catal. Sci. Technol. 7 (8), 1735–1743. doi:10.1039/C6CY02647H.

Lytkina, A.A., Zhilyaeva, N.A., Ermilova, M.M., Orekhova, N.V., Yaroslavtsev, A.B., 2015. Influence of the support structure and composition of Ni–Cu-based catalysts on hydrogen production by methanol steam reforming. Int. J. Hydrog. Energy 40 (31), 9677–9684. doi:10.1016/j.ijhydene.2015.05.094.

Mäki-Arvela, P., Kubickova, I., Snåre, M., Eränen, K., Murzin, D.Y., 2007. Catalytic deoxygenation of fatty acids and their derivatives. Energy Fuels 21 (1), 30–41. doi:10.1021/ef060455v.

Miao, C., Marin-Flores, O., Davidson, S.D., Li, T., Dong, T., Gao, D., Wang, Y., Garcia-Pérez, M., Chen, S., 2016. Hydrothermal catalytic deoxygenation of palmitic acid over nickel catalyst. Fuel 166, 302–308. doi:10.1016/j.fuel.2015.10.120.

Miao, C., Marin-Flores, O., Dong, T., Gao, D., Wang, Y., Garcia-Pérez, M., Chen, S., 2018. Hydrothermal catalytic deoxygenation of fatty acid and bio-oil with *in situ* H_2. ACS Sustain. Chem. Eng. 6 (4), 4521–4530. doi:10.1021/acssuschemeng.7b02226.

Murata, K., Liu, Y., Inaba, M., Takahara, I., 2010. Production of synthetic diesel by hydrotreatment of jatropha oils using Pt–Re/H-ZSM-5 catalyst. Energy Fuels 24 (4), 2404–2409. doi:10.1021/ef901607t.

O'Riordan, T., Sandford, B., 2022. War and the politics of energy and climate change. Environ. Sci. Policy Sustain. Dev. 64 (3), 2–6. doi:10.1080/00139157.2022.2052678.

Orsavova, J., Misurcova, L., Ambrozova, J.V., Vicha, R., Mlcek, J., 2015. Fatty acids composition of vegetable oils and its contribution to dietary energy intake and dependence of cardiovascular mortality on dietary intake of fatty acids. Int. J. Mol. Sci. 16 (6), 12871–12890. doi:10.3390/ijms160612871.

Papageridis, K.N., Charisiou, N.D., Douvartzides, S.L., Sebastian, V., Hinder, S.J., Baker, M.A., AlKhoori, S., Polychronopoulou, K., Goula, M.A., 2020. Effect of operating parameters on the selective catalytic deoxygenation of palm oil to produce renewable diesel over Ni supported on Al_2O_3, ZrO_2 and SiO_2 catalysts. Fuel Process. Technol. 209, 106547. doi:10.1016/j.fuproc.2020.106547.

Peng, B.X., Shu, Q., Wang, J.F., Wang, G.R., Wang, D.Z., Han, M.H., 2008. Biodiesel production from waste oil feedstocks by solid acid catalysis. Process Saf. Environ. Prot. 86 (6), 441–447. doi:10.1016/j.psep.2008.05.003.

Peterson, A.A., Vogel, F., Lachance, R.P., Fröling, M., Michael, J., Antal, J., Tester, J.W., 2008. Thermochemical biofuel production in hydrothermal media: a review of sub- and supercritical water technologies. Energy Environ. Sci. 1 (1), 32–65. doi:10.1039/B810100K.

Qian, Q., Zhang, J., Cui, M., Han, B., 2016. Synthesis of acetic acid via methanol hydrocarboxylation with CO_2 and H_2. Nat. Commun. 7 (1), 11481. doi:10.1038/ncomms11481.

Rashidi, M., Tavasoli, A., 2015. Hydrogen rich gas production via supercritical water gasification of sugarcane bagasse using unpromoted and copper promoted Ni/CNT nanocatalysts. J. Supercrit. Fluids 98, 111–118. doi:10.1016/j.supflu.2015.01.008.

ReadiJet - ARA. https://www.ara.com/products/readijet/ (accessed 2023-03-06).

Roh, H.S., Jun, K.W., Dong, W.S., Chang, J.S., Park, S.E., Joe, Y.I., 2002. Highly active and stable $Ni/Ce–ZrO_2$ catalyst for H_2 production from methane. J. Mol. Catal. Chem. 181 (1), 137–142. doi:10.1016/S1381-1169(01)00358-2.

Samson, K., Śliwa, M., Socha, R.P., Góra-Marek, K., Mucha, D., Rutkowska-Zbik, D., Paul, J.F., Ruggiero-Mikołajczyk, M., Grabowski, R., Słoczyński, J., 2014. Influence of ZrO_2 structure and copper electronic state on activity of Cu/ZrO_2 catalysts in methanol synthesis from CO_2. ACS Catal. 4 (10), 3730–3741. doi:10.1021/cs500979c.

Schiffer, M.A., 2022. War running on fossil fuels. Nat. Hum. Behav. 6 (6), 771–773. doi:10.1038/s41562-022-01398-4.

Stekrova, M., Rinta-Paavola, A., Karinen, R., 2018. Hydrogen production via aqueous-phase reforming of methanol over nickel modified Ce, Zr and La oxide supports. Catal. Today 304, 143–152. doi:10.1016/j.cattod.2017.08.030.

SAF Grand Challenge Roadmap; U.S. Department of Energy, U.S. Department of Transportation. https://www.energy.gov/sites/default/files/2022-09/beto-saf-gc-roadmap-report-sept-2022.pdf.

Tang, T., Jiang, W.J., Niu, S., Liu, N., Luo, H., Zhang, Q., Wen, W., Chen, Y.Y., Huang, L.B., Gao, F., Hu, J.S., 2018. Kinetically controlled coprecipitation for general fast synthesis of sandwiched metal hydroxide nanosheets/graphene composites toward efficient water splitting. Adv. Funct. Mater. 28 (3), 1704594. doi:10.1002/adfm.201704594.

Tian, Q., Zhang, Z., Zhou, F., Chen, K., Fu, J., Lu, X., Ouyang, P., 2017. Role of solvent in catalytic conversion of oleic acid to aviation biofuels. Energy Fuels 31 (6), 6163–6172. doi:10.1021/acs.energyfuels.7b00586.

Vardon, D.R., Sharma, B.K., Jaramillo, H., Kim, D., Choe, J.K., Ciesielski, P.N., Strathmann, T.J., 2014. Hydrothermal catalytic processing of saturated and unsaturated fatty acids to hydrocarbons with glycerol for *in situ* hydrogen production. Green Chem. 16 (3), 1507–1520. doi:10.1039/C3GC41798K.

Wang, Z., Cao, X.M., Zhu, J., Hu, P., 2014. Activity and coke formation of nickel and nickel carbide in dry reforming: a deactivation scheme from density functional theory. J. Catal. 311, 469–480. doi:10.1016/j.jcat.2013.12.015.

Wang, L.X., Guan, E., Wang, Z., Wang, L., Gong, Z., Cui, Y., Yang, Z., Wang, C., Zhang, J., Meng, X., Hu, P., Gong, X.Q., Gates, B.C., Xiao, F.S., 2020. Dispersed nickel boosts catalysis by copper in CO_2 hydrogenation. ACS Catal. 10 (16), 9261–9270. doi:10.1021/acscatal.0c00907.

Yan, S., de Bruin, K., Dennehy, E., Curtis, J., 2021. Climate policies for freight transport: energy and emission projections through 2050. Transp. Policy 107, 11–23. doi:10.1016/j.tranpol.2021.04.005.

Yang, Y., Cheng, D., 2014. Role of composition and geometric relaxation in CO_2 binding to Cu–Ni bimetallic clusters. J. Phys. Chem. C 118 (1), 250–258. doi:10.1021/jp4075674.

Yang, Z., Chen, B., Chen, W., Qu, Y., Zhou, F., Zhao, C., Xu, Q., Zhang, Q., Duan, X., Wu, Y., 2019. Directly transforming copper (I) oxide bulk into isolated single-atom copper sites catalyst through gas-transport approach. Nat. Commun. 10 (1), 3734. doi:10.1038/s41467-019-11796-4.

Yanowitz, J., Ratcliff, M.A., McCormick, R.L., Taylor, J.D., Murphy, M.J., 2017. Compendium of Experimental Cetane Numbers. National Renewable Energy Lab. (NREL), Golden, COUnited States NREL/TP-5400-67585 doi:10.2172/1345058.

Yarmuth, J. A. Inflation Reduction Act of 2022. https://www.congress.gov/bill/117th-congress/house-bill/5376/text.

Yeh, T.M., Hockstad, R.L., Linic, S., Savage, P.E., 2015. Hydrothermal decarboxylation of unsaturated fatty acids over PtSnx/C catalysts. Fuel 156, 219–224. doi:10.1016/j.fuel.2015.04.039.

Zeng, D., Li, Y., Xia, T., Cui, F., Zhang, J., 2022. MOF-derived Co_3O_4 nanoparticles catalyzing hydrothermal deoxygenation of fatty acids for alkane production. ACS Omega 7 (37), 33482–33490. doi:10.1021/acsomega.2c04382.

Zhang, Z., Chen, H., Wang, C., Chen, K., Lu, X., Ouyang, P., Fu, J., 2018a. Efficient and stable Cu-Ni/ZrO_2 catalysts for *in situ* hydrogenation and deoxygenation of oleic acid into heptadecane using methanol as a hydrogen donor. Fuel 230, 211–217. doi:10.1016/j.fuel.2018.05.018.

Zhang, Z., Chen, Z., Gou, X., Chen, H., Chen, K., Lu, X., Ouyang, P., Fu, J., 2018b. Catalytic decarboxylation and aromatization of oleic acid over Ni/AC without an added hydrogen donor. Ind. Eng. Chem. Res. 57 (25), 8443–8448. doi:10.1021/acs.iecr.8b01768.

Zhang, Z., Yang, Q., Chen, H., Chen, K., Lu, X., Ouyang, P., Fu, J., Chen, G.J., 2018c. *In situ* hydrogenation and decarboxylation of oleic acid into heptadecane over a Cu–Ni alloy catalyst using methanol as a hydrogen carrier. Green Chem. 20 (1), 197–205. doi:10.1039/C7GC02774E.

Zhang, S., Yang, X., Zhang, H., Chu, C., Zheng, K., Ju, M., Liu, L., 2019. Liquefaction of biomass and upgrading of bio-oil: a review. Molecules 24 (12), 2250. doi:10.3390/molecules24122250.

Zhang, Z., Jing, M., Chen, H., Okejiri, F., Liu, J., Leng, Y., Liu, H., Song, W., Hou, Z., Lu, X., Fu, J., Liu, J., 2020. Transfer hydrogenation of fatty acids on Cu/ZrO_2: demystifying the role of carrier structure and metal–support interface. ACS Catal. 10 (16), 9098–9108. doi:10.1021/acscatal.0c02320.

Zhao, Y., Zhao, S., Geng, Y., Shen, Y., Yue, H., Lv, J., Wang, S., Ma, X., 2016. Ni-Containing Cu/SiO_2 catalyst for the chemoselective synthesis of ethanol via hydrogenation of dimethyl oxalate. Catal. Today 276, 28–35. doi:10.1016/j.cattod.2016.01.053.

Zhao, Z.W., Zhou, X., Liu, Y.N., Shen, C.C., Yuan, C.Z., Jiang, Y.F., Zhao, S.J., Ma, L.B., Cheang, T.Y., Xu, A.W., 2018. Ultrasmall Ni nanoparticles embedded in Zr-based MOFs provide high selectivity for CO_2 hydrogenation to methane at low temperatures. Catal. Sci. Technol. 8 (12), 3160–3165. doi:10.1039/C8CY00468D.

Zhao, B., Hu, Y., Gao, J., Zhao, G., Ray, M.B., Xu, C.C., 2020. Recent advances in hydroliquefaction of biomass for bio-oil production using *in situ* hydrogen donors. Ind. Eng. Chem. Res. 59 (39), 16987–17007. doi:10.1021/acs.iecr.0c01649.